Available online at www.sciencedirect.com
ScienceDirect
Journal of Marine Systems 66 (2007) 150–160
JOURNAL OF MARINE SYSTEMS
www.elsevier.com/locate/jmarsys

The combined effect of rain and wind on air–water gas exchange: A feasibility study

David T. Ho [a,b,*], Fabrice Veron [c], Emily Harrison [c], Larry F. Bliven [d], Nicholas Scott [e], Wade R. McGillis [a,f]

[a] *Lamont-Doherty Earth Observatory of Columbia University, USA*
[b] *Department of Earth and Environmental Sciences, Columbia University, USA*
[c] *College of Marine and Earth Studies, University of Delaware, USA*
[d] *NASA/WFF, USA*
[e] *Woods Hole Oceanographic Institution, USA*
[f] *Department of Earth and Environmental Engineering, Columbia University, USA*

Received 11 November 2005; accepted 15 February 2006
Available online 22 August 2006

Abstract

A series of experiments were conducted at University of Delaware's Air–Sea Interaction Laboratory to examine the combined effects of rain and wind on air–water gas exchange. During this study, ASIL WRX I, a combination of 3 rain rates and 4 wind speeds were used, for a total of 12 different environmental conditions. The SF_6 evasion method was used to determine the bulk gas transfer velocities, and airside profiles of wind and CO_2 were used to estimate flux–profiles of momentum and carbon dioxide. In addition to measurements of fluxes with and without rain in a wind–wave boundary layer, measurements of wave properties were also obtained. Rain is shown to alter the wind profile in the flume, and dampen surface waves. Also, SF_6 evasion indicates that with the present experimental setup, for most of the experimental conditions, rain and wind combine linearly to influence air–water gas exchange. Flux–profile relationships for marine atmospheric boundary layers, which were performed to scale up to field measurements, were explored by a comparison between SF_6-derived bulk fluxes and airside CO_2 profile measurements.

1. Introduction

Air–water gas exchange is an important process on local, regional, and global scales as it determines evasion of volatile pollutants, aqueous dissolved oxygen content, and cycling of biogeochemically important trace gases. Gas exchange for slightly soluble gases is thought to be controlled predominantly by subsurface turbulence, which is in turn driven by environmental processes such as wind, rain, waves and other processes affecting subsurface mixing.

The effect of wind on gas exchange has historically received a great deal of attention, where many laboratory and field experiments have been conducted, and parameterizations between wind and gas exchange developed. Recently, the relationship between rain and gas exchange has been examined in a series of laboratory experiments, in both freshwater (Ho et al., 1997)

* Corresponding author. Lamont-Doherty Earth Observatory of Columbia University, USA.
E-mail address: david@ldeo.columbia.edu (D.T. Ho).

0924-7963/$ - see front matter © 2006 Elsevier B.V. All rights reserved.
doi:10.1016/j.jmarsys.2006.02.012

and saltwater (Ho et al., 2004) environments. Furthermore, the mechanisms responsible for the gas exchange enhancement have been determined (Ho et al., 2000). However, thus far, the interaction between rain and wind, and how they combine to influence air–water gas exchange has not been studied.

In the following, results are presented for a series of experiments conducted at University of Delaware's Air–Sea Interaction Laboratory as part of ASIL WRX I. The SF_6 evasion method was used to determine the bulk gas transfer velocities. Airside measurements of wind and CO_2 were used to examine the momentum and gas flux–profile relationships under wind and rain conditions. Flux–profile relationships (McGillis et al., 2001) for marine atmospheric boundary layers were explored by comparing bulk gas fluxes from SF_6 and atmospheric gradient measurements from CO_2.

2. Methods

During ASIL WRX I, 12 environmental conditions were conducted with a combination of 3 rain rates and 4 wind speeds (including null cases; see Table 1 for details). Water side SF_6, as well as airside CO_2 measurements were made to determine the gas transfer velocity, and to examine the marine atmospheric boundary layers during rain. Physical measurements of rain, wind, and waves were also made.

2.1. Air–sea interaction laboratory

The experiments were conducted in a wind–wave–current flume, situated in the University of Delaware's Air–Sea Interaction Laboratory in Lewes, Delaware. The flume is a 1 m wide, 1.25 m high, and 42 m long, with a 37 m long working section. Water depth is generally kept at 0.71 m to allow sufficient air space above the water surface, but can be varied from 0.2 to 1 m. The flume is equipped with a programmable plunging-wedge wave maker, which allows for the computer-controlled generation of mechanical wave packets. An artificial beach is placed at the end of the flume to dissipate wave energy and eliminate wave reflections. The recirculating wind tunnel is a capable of up to 17 m s^{-1} wind speed (in the centerline of the air space, equivalent to approximately 24 m s^{-1} at 10 m) at normal operating water depth. Air humidity and temperature, and water temperature are also independently controllable and can be set from 5 to 40 °C. The water temperature during the experiment averaged about 17.5 °C. Currents up to 0.5 m s^{-1} can be generated in the flume using a recirculating pump. Both the wind and current speed are computer-controlled and fully programmable.

Table 1
ASIL WRX I experimental summary

Experiment	Water temp. (°C)	Wind speed (m s^{-1})	Rain rate (mm h^{-1})			k(600) (cm h^{-1})
			Tank overflow	Bucket rain gauge	RIS[a]	
1	17.0	4.0	0.0	0.0	0.0	2.6±0.2
2	17.1	3.8	30.2	29.9	33.3	11.7±0.3
3	17.4	8.1	0.0	0.0	0.0	9.8±0.6
4	17.2	7.6	25.6	29.0	31.8	15.5±0.3
5	16.8	12.5	30.5	29.0	33.2	29.5±0.3
6	17.0	12.8	0.0	0.0	0.0	20.5±0.5
7	17.3	0.0	24.7	29.3	34.1	7.9±0.5
8	17.7	0.0	15.3	11.1	22.0	5.1±1.1
9	17.9	0.0	0.0	0.0	0.0	0.7±0.4
10	17.8	12.5	11.1	12.0	16.7	26.4±0.4
11	17.9	3.9	10.2	11.1	16.7	5.6±0.6
12	17.7	7.9	13.9	11.7	18.4	13.5±0.3

[a] Error on the Rain Imaging System (RIS) measurements is ca. 12%.

2.2. Experimental design

During ASIL WRX I, a portion of the roof near the center of the wind–wave–current flume was open, and a rain simulator was placed 2.6 m above the water surface over the open portion (Fig. 1). The rain simulator measured 1.4 × 0.9 m, and was equipped with 6922 20-gauge hypodermic needles. Different rain rates were generated by changing the number of needles. For ASIL WRX I, 0, 1800, and, 6922 needles were used, providing no rain, and nominal rain rates of 11 and 30 mm h^{-1}, respectively.

Groundwater was stored in two large reservoirs in the laboratory, and used to supply the rain simulator. The water was stripped of excess trace gases commonly found in groundwater (e.g., CO_2, CH_4, N_2O) by bubbling atmospheric air through the water using a 10-m length of microporous tubing. From the reservoirs, the water was pumped to the rain simulator, and overflow from the constant head was returned to the reservoir while the rest rained on the water surface inside the wind–wave–current flume. The water level inside the flume was kept at a constant height with a standpipe that drained to a 200-L container, which was then emptied manually. Quantifying the volume of the containers emptied during an experiment provided a measure of the average rain rate.

Experiments with nominal wind speeds, scaled to 10 m height, u_{10}, of 0, 4.0, 8.0, and 12.5 m s^{-1} (measured in the air–space center line) were

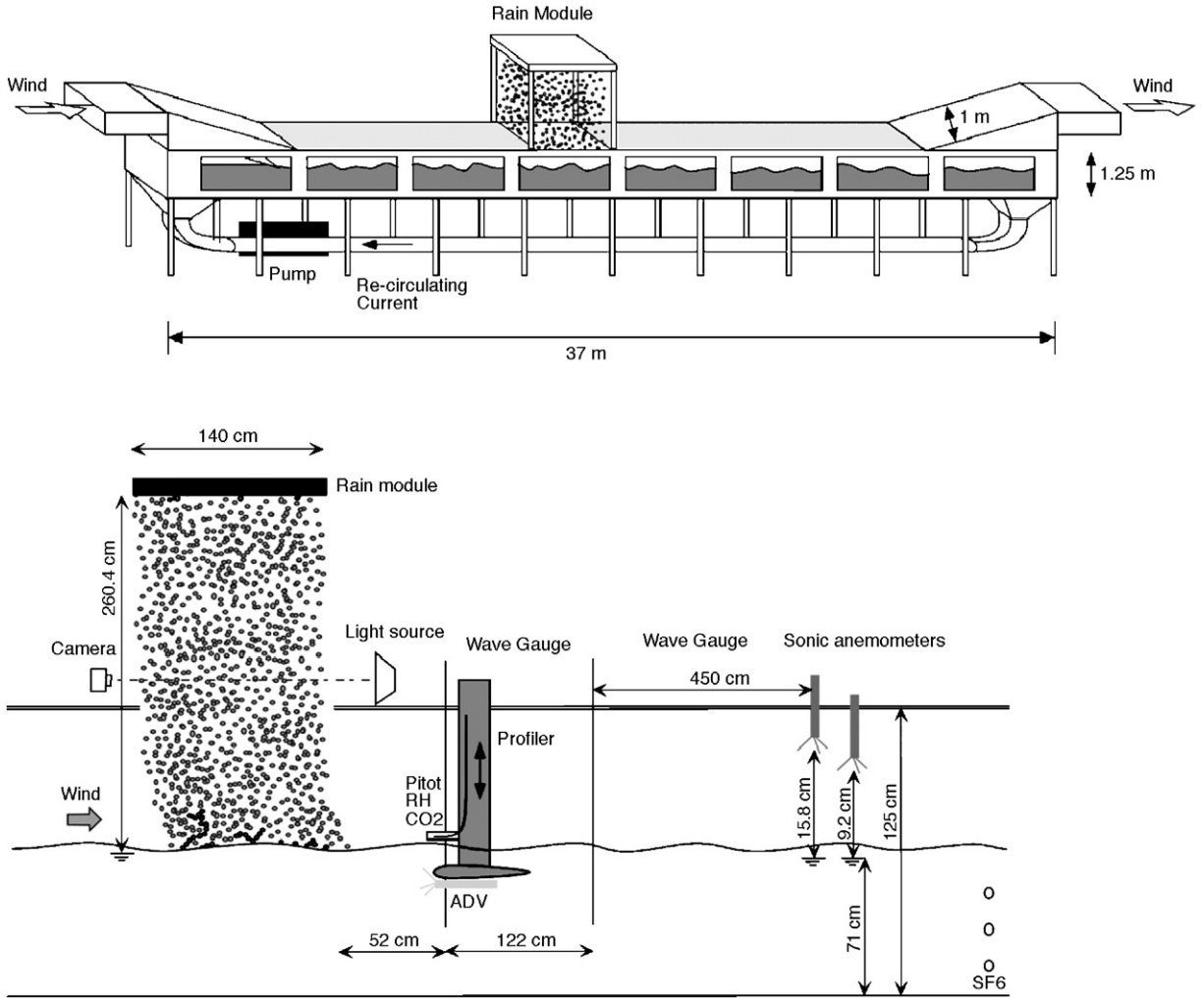

Fig. 1. Schematic diagrams of the laboratory setup during ASIL WRX I.

performed. Wind and currents were computer controlled and were steady and repeatable. Together with the 3 rain rates studied, a total of 12 experiments were performed. Each lasted approximately 3 h during which wind velocity profiles, wave height, rain rates, water velocity profiles, aqueous SF_6 concentration, and airside CO_2 profiles were measured. A steady current of ca. 3 cm s^{-1} was set up in the flume to provide homogenization for the SF_6 measurements.

2.3. Rain rate and drop size measurement

During ASIL WRX I, rain rates were measured by using a bucket rain gauge, by measuring the water overflow from the flume, and by using NASA's Rain Imaging System (RIS). Additionally, RIS was used to measure the drop size distributions.

Typical operation conditions for RIS are described by Ho et al. (2004), but two modifications to the software were required to analyze the ASIL WRX I data. First, the localized rain rates, during ASIL WRX I, were more intense than those of natural observations. Hence, multiple drops within an image were sometimes observed to overlap, leading to incorrect estimates of drop sizes, and consequently, rain rates. The software was modified to reduce this unwanted feature. To identify drops, the image processing software used edge detection, followed by thresholding. Increasing the threshold reduced the depth of field, yet the relationship was unknown. Twelve hours of RIS data from hurricane Isabel were used to derive a scaling relationship between depth of field and threshold level. For the ASIL WRX I data, a threshold level that reduced the depth of field by a factor of 4.2 compared to the natural

algorithm was used. The threshold modification increased the maximum rain rate of RIS observations from about 300 to 1200 mm h^{-1}, and for the highest rain rate during ASIL WRX I, there was typically less than one drop per image. The second modification was for the drop vertical velocity. In nature, drop velocities at ground level are well approximated by their terminal velocity. During ASIL WRX I, the rain simulator was 2.6 m above the water surface, a distance that was insufficient for the drops to reach terminal velocity. Fall velocity was estimated using a method proposed by Craeye (1998), which accounts for the change in raindrop shape as it falls through the air.

2.4. Wind speed

Wind speed in the flume was measured with a Pitot tube and two 2-D sonic anemometers (Fig. 1). The two sonic anemometers were placed 6.24 and 6.44 m downwind of the rain module in the centerline of the flume, and 15.8 cm and 9.2 cm from the still water level. The Pitot tube was placed on a profiler and 52 cm downwind of the rain module. Data from the Pitot tube was sampled using the A/D board described below at 200 Hz. Because the Pitot tube dynamic pressure port is normal to the streamwise flow, rain and spray droplets covered the port opening and reduced the accuracy of wind measurements under rain conditions. Therefore, wind speeds reported in this study are from acoustic non-invasive techniques.

2.5. SF_6 evasion experiments

A series of SF_6 evasion experiments was used to determine the gas transfer velocity. Because of the sensitivity of GC-ECD for detection of SF_6, only three tracer injections were necessary for the whole of ASIL WRX I. At the beginning of experiments 1, 5, and 8, ca. 9 pmol (pmol = pico mol = 10^{-9} mol) of SF_6 dissolved in water was injected into the flume upwind of the rain module using a 60-ml plastic syringe.

Then, at 15-min intervals, SF_6 samples from 3 different depths at one location in the flume (Fig. 1) were taken through lengths of 0.3175 cm ID flexible vinyl tubing with 50 ml glass syringes. During a typical sampling procedure, the glass syringe was connected to a 3-way valve at the end of the vinyl tubing, and the valve was opened and water was drawn slowly into the syringe. Extreme care was taken to prevent the occurrence of bubbles in the sampling line or in the syringe, and no samples were kept for analysis when bubbles were seen in the tubing or in the syringe.

The samples were analyzed using a headspace method described in detail by Wanninkhof et al. (1987). A predetermined amount of water (10 to 30 ml) was drawn into the syringe during sampling, and then a headspace (40 to 20 ml) was created with ultra-high purity (UHP; 99.999%) N_2. Then, after at least 3 min of vigorous shaking on a mechanical wrist-action shaker to equilibrate the water with N_2 in the headspace, the gas sample was pushed through a drying column of $Mg(ClO_4)_2$ into a sample loop. Subsequently, the sample was injected into a GC-ECD using UHP N_2. SF_6 was separated from other gases at room temperature using a molecular sieve 5A column.

2.6. Tracer dilution models and gas exchange calculations

The gas flux across the air–water interface, F, is related to the total change in mean SF_6 concentration in the flume with time by:

$$F = h\frac{dC}{dt}, \tag{1}$$

where h is the mean depth of water in the flume. The gas transfer velocity, k, is described by:

$$k = \frac{F}{(C_w - \alpha C_a)}, \tag{2}$$

where C_w is the SF_6 concentration in the water directly below the air–water interface, and αC_a is the solubility equilibrium for SF_6 in the water. If the water is well mixed with respect to tracer concentration, Eqs. (1) and (2) are combined, assuming that $C_w = C$, and integrating over Δt to obtain:

$$k = \frac{h}{\Delta t}\ln\frac{(C_i - \alpha C_a)}{(C_f - \alpha C_a)}, \tag{3}$$

where C_i and C_f are the initial and final mean tracer concentrations, respectively.

The observed decrease in total tracer concentration in the water during the experiments was caused by gas exchange at the air–water interface and by dilution of tank water by nominally SF_6-free rain. In order to calculate k, the effect of dilution must be removed. This can be accomplished by a dilution model described in detailed in Ho et al. (2000, 1997):

$$k = \frac{h}{\Delta t}\ln\frac{(C_i - \alpha C_a)}{(C_f - \alpha C_a)} - \frac{hP}{V} \tag{4}$$

where P is the rain volume rate, and V is the volume of the flume.

The gas transfer velocity for SF_6 was normalized to a Schmidt number (Sc) of 600, corresponding to values for CO_2 at 20 °C using the relationship:

$$k(600) = k_{SF_6}\left(\frac{600}{Sc_{SF_6}}\right)^n, \quad (5)$$

where k_{SF_6} and Sc_{SF_6} are the gas transfer velocity and the Schmidt number for SF_6 (782 for our experiment), respectively. Sc for a particular gas is defined as the ratio of the kinematic viscosity of water, to the diffusion coefficient of that gas in water. It has been shown in models and experiments that for a clean wavy water surface, in the absence of bubbles, n equals − 1/2 (Brumley and Jirka, 1988; Jähne et al., 1984; Ledwell, 1984).

2.7. Waves

Waves in the flume were measured with capacitance gauges and the signal sampled at 200 Hz with a 16-bit A/D board on a PC. A total of 3 wave gauges were sampled (one upwind of the rain module and two downwind; see Fig. 1). The wave gauge data presented here were taken from the wave gauge located 1.74 m down wind of the rain module. The wave gauge was placed in the centerline of the flume and calibrated before and after each experiment. No drift in the calibration was observed. Spectra of the wave height were calculated for 9-min-long records (108,000 points) using Hanning windows of 10.24 s (2048 points) with a 50% overlap. Each experiment provided 162 min of wave gauge data. It was found that the wave field did not vary during the experiments and 9-min-long records were therefore sufficiently representative of the wave conditions.

2.8. Atmospheric CO_2 profiles

It is necessary to develop flux–profile relationships under rain conditions in order to measure rain-induced air–water gas fluxes in the field. For a surface flux of a scalar X under rain conditions, the flux–profile relationship can be expressed as:

$$F_X = \frac{u_* \kappa}{\varphi_R}\frac{\partial X}{\partial(\ln z)} \quad (6)$$

where F_X is the surface flux of X, u_* is the friction velocity, κ is the von Karman constant, φ_R is the flux–profile correction for a rain-influenced atmospheric boundary layer, and z is the height above the mean water surface. CO_2 profiles are measured with two non-dispersive infrared (NDIR) analyzers in the atmosphere above the flume. The technique to resolve small vertical gradients of atmospheric CO_2 using two NDIR analyzers is described in McGillis et al. (2001). One NDIR detector is used to measure the time varying CO_2 in the headspace of the flume at a fixed position. A second NDIR detector is used to measure the atmospheric profile of CO_2 from an intake on the vertical profiler. Continuous differences between the profiled and fixed gas concentrations remove the horizontal and temporal changes in gas concentration. These temporal changes are larger than the vertical gradients. The differencing method provides the precision in the profile data to perform the flux–profile technique. This method increases the accuracy in the flux–profile technique for momentum, heat, and gas.

2.9. Turbulence from ADV

An acoustic Doppler velocimeter (ADV) was positioned at different depths over the course of the experiment to obtain profiles of the kinetic energy dissipation rate ε, via the inertial subrange of the velocity spectra. However, the data obtained did not lend themselves to the calculation because of the lack of particles in the water, and the low current velocity in the tank.

3. Results and discussion

3.1. Rain rates and drop size distribution

Rain rates were measured using three different methods as described above, and the results are summarized in Table 1. The rain rate measured at the rain simulator, which covered an area of 1.21 m^2, was scaled by the surface of the flume (39.24 m^2) to derive a spatially averaged rain rate. There is general agreement amongst the methods, however no technique is ideal, and here are some of the factors that contribute to uncertainties in each method: 1) The overflow method relies on accurate measurements of the elevation of a calm water free surface at the start and end of each experiment, as well as accurate measurements of the overflow; 2) The bucket rain gauge relies upon an assumption that the bucket measurement site is representative of the entire rain simulator, and that the rain rate measured at a given time is representative of the entire duration of the experiment; 3) RIS algorithms were developed for natural rain that is randomly distributed in both space and time. The rain simulator has a regular grid pattern and the drop drip rate is not random, hence the RIS rain rates are likely to have greater than the usual 5% error.

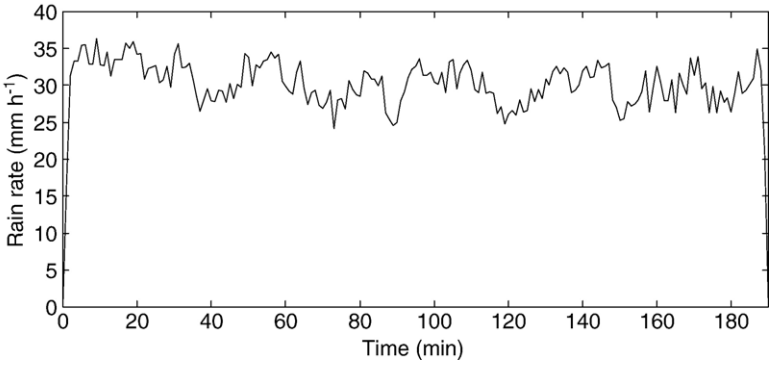

Fig. 2. Rain rate as a function of time during Experiment 5 measured by RIS. The mean is 33.2 mm h^{-1}, and the standard deviation is 4.0 mm h^{-1}. The variability in rain rate is typical of all the experiments.

RIS estimates of the rain rate R for each minute during the experiments show that the relative variability is on the order of 12% (Fig. 2). Spectral analysis indicates dominant and minor peaks at about 38 and 13 min. The exact cause is not known, but could be a result of nonlinear interaction between the flow rates of the pump (pumping the water up to the rain module), which is subject to a decreasing head in the reservoir, the needle drip flow, and the overflow that provides a constant head above the needles. Due to the variability, measurements over an extended period are needed to improve estimates of the average R. The bucket measurements of R were obtained from 1 min of data. On the other hand, RIS measurements were obtained for the full duration of the experiments, but the RIS measurement area was only a small fraction of the simulated rain area. Thus the overflow technique was used as the best estimate of the average rain rates because this method obtained data (a) during the entire experiment and (b) the collection area included the entire rain simulator area.

Drop size distributions from RIS during ASIL WRX I have a narrow-banded shape because the 20-gauge needles in the rain simulator produced raindrops with mean diameter of 2.1 mm and a standard deviation of 0.07 mm. Fig. 3 shows the DSD for Experiment 5, for which RIS estimated R to be 33.2 mm h^{-1}. On the other hand, natural rainfall distributions have a logarithmically decreasing shape that is often modeled by the Marshall-Palmer DSD (Meneghini and Kozu, 1990). The Marshall-Palmer DSD for a rainfall rate comparable to Experiment 5 is also displayed in Fig. 3.

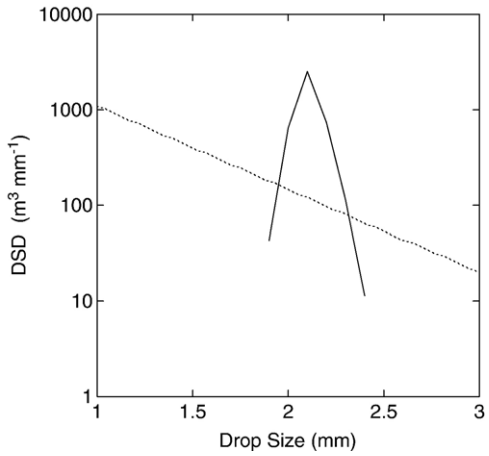

Fig. 3. Typical raindrop size distribution (DSD) as measured by RIS during ASIL WRX I (solid line). Although the DSD for the simulated rain was narrow banded compared to the logarithmically shaped DSD of a natural rain with a similar rain rate (dotted line; approximated by the Marshall-Palmer distribution), the two DSDs produced similar KEFs.

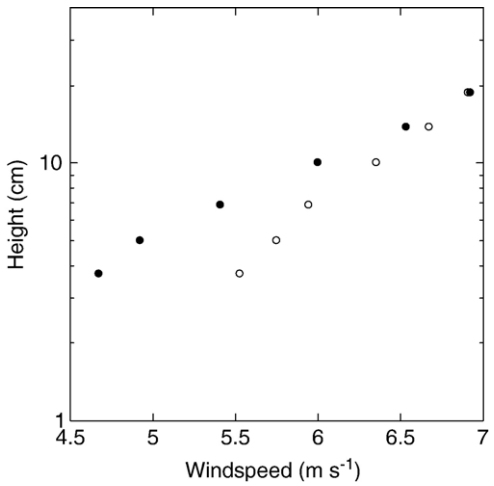

Fig. 4. Wind profiles measured with a sonic anemometer at the highest wind speed, and under rain (solid symbols) and no rain conditions (open symbols).

Table 2
Reduction in wind speed due to rain

	No rain, 0 mm h^{-1}	Low rain, 10.2–15.3 mm h^{-1}	High rain, 24.7–30.5 mm h^{-1}
No wind, 0 m s^{-1}	0.0	0.0	0.0
Low wind, 3.8–4.0 m s^{-1}	4.0	3.9 (2.5%)	3.8 (5%)
Mid wind, 7.6–8.1 m s^{-1}	8.1	7.9 (2.5%)	7.6 (6.2%)
High wind, 12.5–12.8 m s^{-1}	12.8	12.5 (2.3%)	12.5 (2.3%)

The numbers in parenthesis indicate percentage reduction in wind speed.

The shapes of the DSDs are quite different. Yet the kinetic energy fluxes (KEF) are the same order of magnitude ($KEF_{ASIL}/KEF_{natural} \sim 0.45$), so the simulated rain produces a practical alternative for this study. KEF from the raindrops was computed using the overflow rain rate measurements, the RIS drop size measurements, and the rain simulator to wave-tank area scaling factor.

3.2. Wind speed

When the rain rate was high, the amount of water falling through the air caused momentum to transfer from the wind to the rain. This caused the wind speed to slow down (Fig. 4; Table 2) and decreased the wind-induced stress, but added a horizontal component to the rain. For example, using the wind velocity profiles shown in Fig. 4, the momentum deficit caused by rain was calculated to be ~ 8.5% of the total wind momentum. The horizontal component of the rain was not accounted for when considering the KEF input to the water. This horizontal component of the drop velocity can however carry a significant fraction of the total stress. In fact, in the field, one can consider that the droplets horizontal impact velocities is approximately 85% of the 10-m wind speed (Caldwell and Elliott, 1971), then the stress carried by the rain is $\tau = 0.85\rho R u_{10}$, where ρ is the density of the droplets. This can be significant compared to the wind stress, especially at low wind speeds since the wind stress is quadratic with u_{10} and is dominant at high wind speeds.

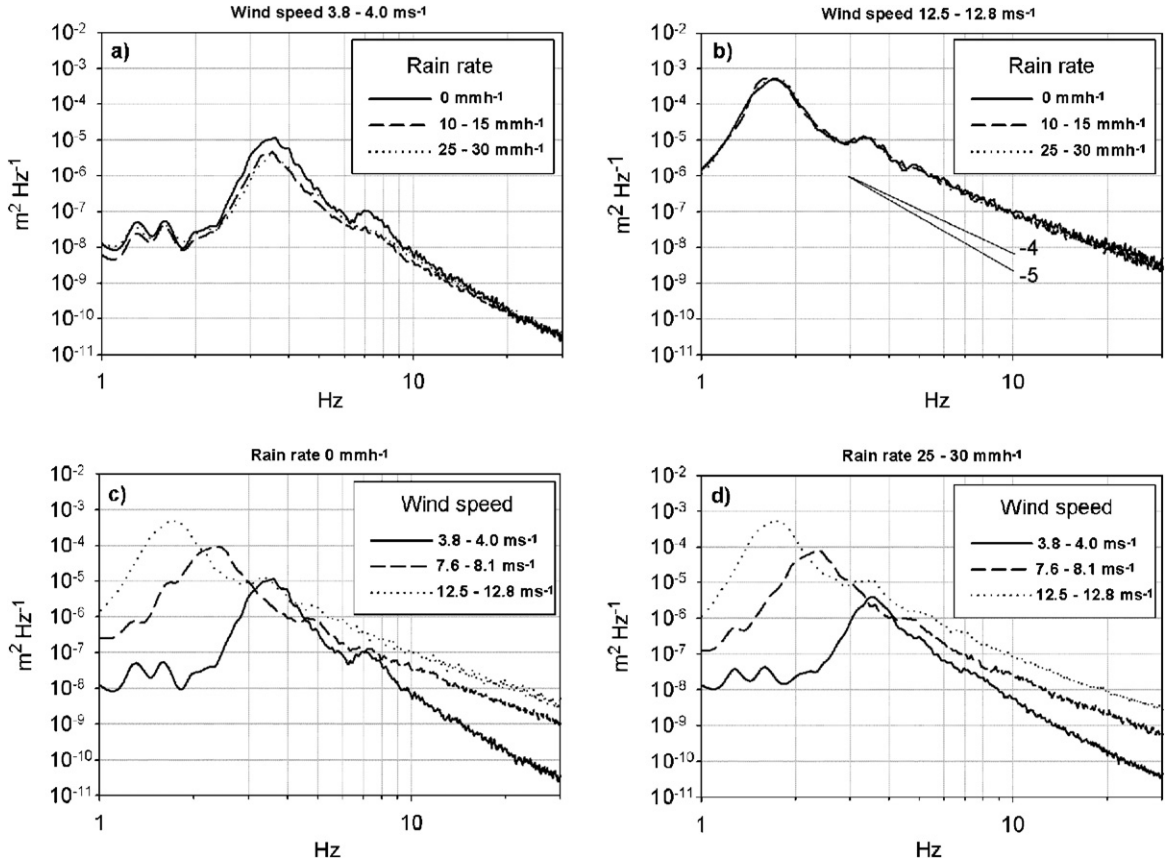

Fig. 5. Spectra of the wave height at 174 cm downwind of the rain simulator. a) The wave height spectra for the lowest wind speed under varying rain conditions. Note that the waves are attenuated by the rain. b) The effect of the rain becomes undetectable at high wind speed. c) The wave height spectra for all wind speeds with no rain. d) The spectra for all wind speeds under the highest rain conditions.

Here, despite the decrease in wind speed, the overall horizontal momentum transferred to the water surface is most likely similar as the decrease in wind stress is counteracted by the increase in momentum carried by the drops upon impact.

Furthermore, wind-induced air–water gas exchange is driven by turbulence transferred from wind to the air–water surface through shear, wave drag, wave breaking, and subsequent bubble formation. In the presence of wind, rain might further enhance wind-induced gas exchange because even though wind loses some of its momentum to rain, the raindrops impacts the air–water interface and generate mechanisms on scales that are closer to the scales of mixing controlling air–water gas exchange. For this reason, the presence of rain and wind may result in an efficient condition for enhancing air–water gas exchange beyond that of each individual process occurring separately.

3.3. Waves

Fig. 5 shows spectra of the wave height at 174 cm downwind of the rain simulator. The spectra appear significantly reduced at high rain rate for the lower wind speed (Fig. 5a), and over the full spectrum. At this wind speed, the peak of the spectrum (3–4 Hz) is damped by a factor of 5. At the highest wind speed, the effect of the rain is essentially not visible (Fig. 5b). These results are consistent with previous results of wave damping by the rain (Poon et al., 1992; Tsimplis and Thorpe, 1989; Tsimplis, 1992; Yang et al., 1997) where it is believed that the waves are viscously damped while propagating over the rain generated turbulence. However, viscous damping would damp the high frequency waves the most. Yet, for the lowest wind speed condition studied here, the full range of frequencies, at least up to 20 Hz, appears to be damped. This is a departure from previous results, and is perhaps caused by the reduced wind speed (see Fig. 4) under this high rain rate condition, which would in turn provide less wind stress toward the generation of surface waves. Also, Fig. 5c and d show the wave spectra under constant rain condition for varying wind speeds. As expected, the wave peak downshifts from 3.5 Hz at the lowest wind speed, to approximately 1.8 Hz at the highest wind speed. Also, the tail of the spectrum appears to fall off with a slope of −5 at the lowest wind speed and a slope of −4 at the highest wind speed.

3.4. Gas transfer velocities from SF_6

For wind-induced gas exchange, the dominant mechanism is turbulence induced by wind waves. For rain, it is turbulence produced by impact of raindrops on the water surface. Bubbles play a role for both processes under certain circumstances (Asher and Wanninkhof, 1998; Ho et al., 2000). Besides the individual mechanisms contributed by rain and wind, several processes caused by the interaction of both might be important, and they affect k(600) differently. First, bubble production by rain and then injection by wind-waves would enhance k(600). Second, dampening of wind waves by rain could decrease the production of near surface turbulence, leading to decreased k(600). Third, intense rain falling through the headspace above the tank leads to the transfer of momentum from wind to rain, which would decrease the wind waves but increase the KEF from the rain drops. At this point, it is not clear if this interaction would increase or decrease k(600).

The results of the two experiments conducted with rain and no wind are consistent with previous rain experiment results reported in Ho et al. (2000, 1997), indicating that scaling via KEF is reasonable even when rain drops do not achieve terminal velocity (Fig. 6). k(600) results from all 12 experiments are shown in Fig. 7. As expected, the gas transfer velocity, k(600), increased with both rain rate and wind speed. At the same windspeed, k(600) increased linearly with increasing rain rate, but at the same rain rate, k(600) increased as a nonlinear function of increasing wind speed (Fig. 7).

The simplest assumption about the combined effect of rain and wind on gas exchange is that they are additive. To assess this assumption, a simple model that predicts the combined effect of rain and wind on gas exchange could be used. The model is constructed based

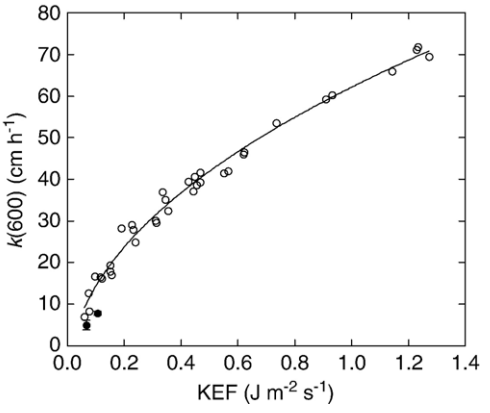

Fig. 6. Results of laboratory experiments on rain-induced gas exchange from NASA's Rain Sea Interaction Facility (open symbols, from Ho et al., 2000, 1997) and ASIL WRX I (solid symbols). The comparison shows that scaling using KEF is reasonable, even when raindrops are not at terminal velocity.

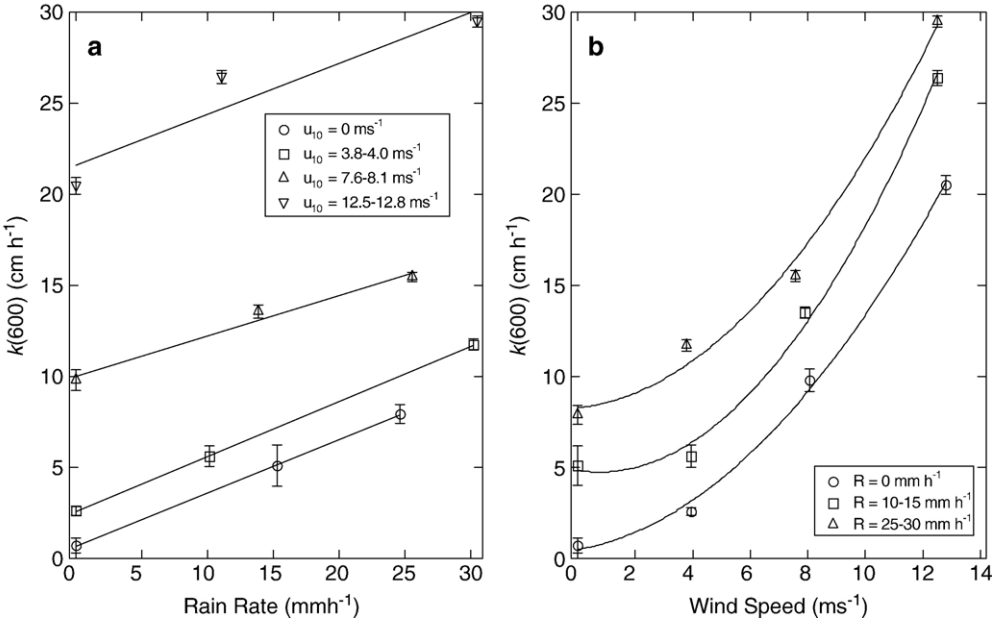

Fig. 7. $k(600)$ results from SF_6 evasion experiments. a) At the same wind speed, $k(600)$ increased linearly with increasing rain rate; b) but at the same rain rate, $k(600)$ increased as a non-linear function of increasing wind speed.

on $k(600)$ from the null experiments at ASIL WRX I, combining a linear fit to the rain data, and a second order polynomial fit to the wind data. The model can be described by the following equation:

$$k(600) = 0.511 + 0.296R + 0.261u_{10} + 0.102u_{10}^2. \quad (7)$$

The model and data are compared in Fig. 8. The model was further compared with an empirical multi-parameter fit of all data to an equation of the form of Eq. (7) (Burke Hales, pers. comm.). The fit was determined by minimizing the average relative absolute difference (ARAD) between data and fitting function, using Powell's method (Press et al., 1989). The empirical fit of all data was only slightly better than the additive model (ARAD of 1.5 for empirical fit, compared to 1.6 for the parameters of Eq. (7)), and the values of the fitting coefficients were only slightly different than those of the model. The comparison between model and data implies that with the present experimental setup, the combined effect of rain and wind is approximately linearly additive.

There is one experiments (Exp. 10) where this does not seem to be true, at the highest wind speeds, and mid rain. In this case, the combined effect seems to increase the gas transfer velocity more than the addition of the two individual processes. It is possible that this is just an experimental outlier. However, it is also possible that at the higher rain rates and wind speeds, enhancement due to bubbles is more important, due to entrainment of bubbles to greater depths by wind waves. Yet, this effect might be offset at high rain rates by the interference

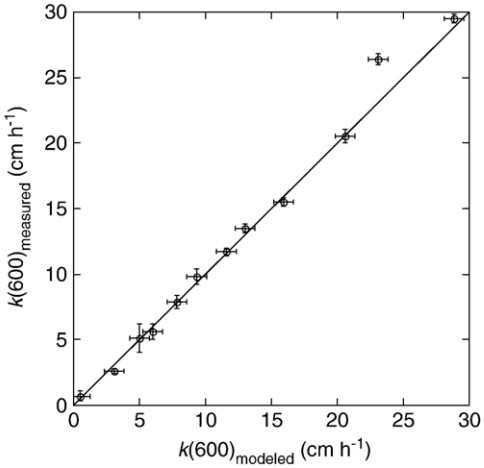

Fig. 8. Comparison between the modeled and measured $k(600)$ from ASIL WRX I. The model is based on the null experiments, and has an error of ± 0.75 cm h^{-1}. For most of the experiments, the model, which assumes that the effects of rain and wind are additive, is able to reproduce the data. The one case where this is not true is at high winds and mid rain. Without more extensive measurements of the underlying mechanisms, it is not possible to determine whether the point is an outlier, or the result of non-linear interactions between different mechanisms produced by rain and wind.

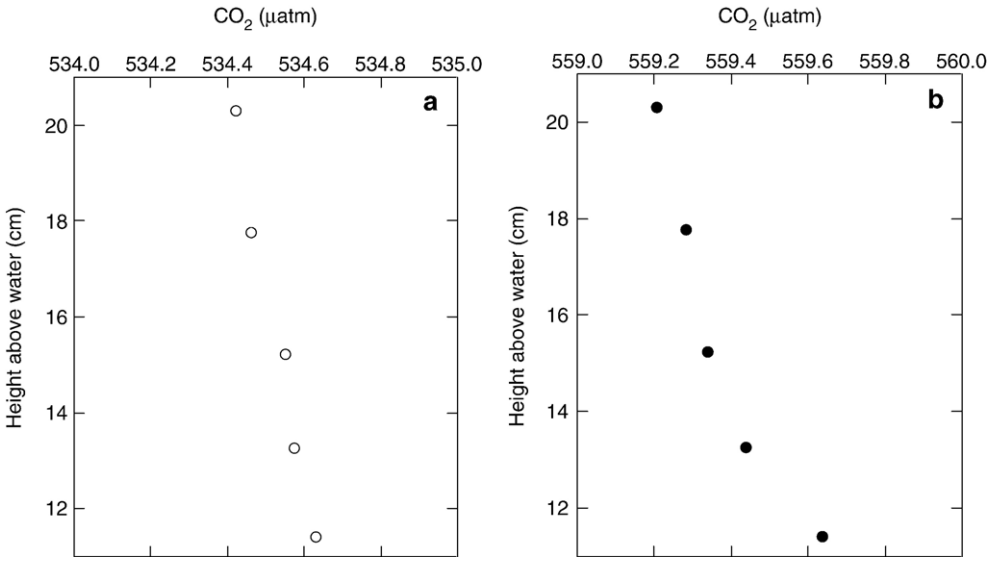

Fig. 9. Carbon dioxide profiles measured with non-dispersive infrared (NDIR) analyzers in the atmosphere above the flume. Data are for a) no rain (open circles) and b) rain conditions (solid circles). The wind speeds were 12.8 and 12.5 m s^{-1}, respectively for a) and b), and rain rate was 30.5 mm h^{-1} for b).

between rain and wind waves, which leads to dampening of wind waves by rain. In order to quantify these effects, more detailed measurements of turbulence and bubbles need to be performed.

3.5. CO_2 profiles

Fig. 9 shows CO_2 profiles measured using the difference between two NDIR analyzers in the air above the flume. Experimental measurements are shown for no-rain and a rain rate of 30.9 mm h^{-1}. The windspeed was nominally the same (12.5 and 12.8 m s^{-1}) for both cases shown in Fig. 9. During each experiment, the dissolved CO_2 in the water was reduced due to evasion. Typical starting values of pCO_2 in the water were near 1500 µatm and 500–600 µatm in the air. The water pCO_2 decreased to approximately 1000 µatm over the course of an experiment. Airside CO_2 concentrations remained nominally constant.

The calculation of the air–water CO_2 flux using the atmospheric profile method begins with measurements of $\partial CO_2/\partial(\ln z)$ downwind of the rain simulator. The gas transfer velocity in the rain region of the tank, $k(600)_R$, is approximated from an area-weighted average of the gas transfer velocities measured during rain and no-rain conditions using the formulation:

$$k(600)_{\text{total}}A_{\text{total}} = k(600)_{\text{NR}}A_{\text{NR}} + k(600)_{\text{R}}A_{(\text{R})} \qquad (8)$$

where $k(600)_{NR}$ is the gas transfer velocity in the part of the flume not impacted by rain, $k(600)_R$ is the gas transfer velocity in the rain footprint. A_{total} and A_R are the total flume surface area, and the area of the rain footprint, respectively. A_{NR} is the area outside the rain footprint (i.e., $A_{NR}=A_{total}-A_R$). $k(600)_{total}$ and $k(600)_{NR}$ were determined from the total SF_6 transfer velocities over A_{total} during rain and no rain conditions, respectively, using Eq. (5) and the appropriate Sc for SF_6 at the environmental conditions. Solving Eq. (7), $k(600)_R$ is estimated to be 257.3 and 136.2 cm h^{-1} for rain rates of 30.5 and 11.1 mm h^{-1}, respectively. There are a couple of possible limitations that should be mentioned concerning this calculation. The actual rain-influenced surface might be larger than A_R, because of the horizontal momentum imparted on the raindrops by wind. Also, these $k(600)_R$ estimates include both the effects of wind and rain. To obtain an estimate of the rain-only contribution to $k(600)_R$, the wind-only effect, approximately 20 cm h^{-1} from Experiment 6, should be subtracted from these wind and rain values. Using the relationship between KEF and $k(600)$ described in Ho et al. (1997), the predicted $k(600)$ are 133 and 78 cm h^{-1} for the high and low rain rates, respectively. These values are for a system without wind, and may explain some of the reduction.

In order to examine the systematic effects of rain and wind on gas exchange in the natural environment, logistically, meteorological techniques hold the most promise. With tracer, there is the safety issue of sampling in a thunderstorm. Hence, one of the goals of this investigation was to explore the feasibility and applicability of the flux–profile techniques to measure the air–water flux of gases under rain and wind conditions.

The structure of turbulence in the atmospheric boundary layer is likely to be altered significantly by rain, resulting in an altered vertical turbulent transport of momentum, heat, and gas. Therefore, it is crucial to understand the vertical fluxes during wind and rain in both the atmosphere and water. An important component of this contribution is to ascertain the modifications to the flux–profile relationships under these environmental conditions. To develop a flux–profile relationship for rain from this study, the gas fluxes derived from SF_6 mass balance were set equal to the flux–profile relationship:

$$F_{SF_6} = \frac{u*\kappa z}{\varphi_R}\frac{\partial c_{CO_2}}{\partial z} = k\Delta\ CO_2 \quad (9)$$

Using $k(600)_R$ estimated from the experiments in this study, φ_R, is determined to be 0.17 and 0.4 for rain rates of 30.5 and 11.1 mm h^{-1}, respectively.

4. Summary

The experiments conducted as part of ASIL WRX I show that on first order, rain and wind combine linearly to enhance gas exchange in freshwater. The experiments also show that it should be feasible to use flux–profile techniques to measure the air–water gas fluxes in the field under rain and wind conditions, provided that the flux–profile relationship is known.

However, two important limitations of the experiments need to be kept in mind: 1) During ASIL WRX I, rain was very localized, and therefore the physics might not be realistic; 2) There was no interaction between rain and wind over most of the flume area, and the potential effect of raindrops in dampening wind waves did not occur over much of the tank. The fact that the rain was localized may have prevented significant non-linear interactions between rain and wind, and between the rain and waves, leading to the apparent linear addition of the wind and rain effects on the gas transfer.

In order to provide definitive statements about the combined effect of rain and wind on air–water gas exchange, some of the physical mechanisms responsible for the rain and wind enhancement, and the interaction between waves, turbulence, and bubbles produced by wind and rain remain to be examined. For follow-up investigations, efforts should be made to cover the entire surface of the flume with the rain simulator. In this case, the physical processes will be more realistic. Also, measurements of turbulence with particle image velocimetry (PIV), raindrops with laser Doppler velocimetry (LDV), and also bubbles should be accomplished.

Acknowledgment

We thank J. Bent, L. Lenain, M. Stellato, and H. Tang for assistance during the experiment, and A. Pineda Rojas for assistance with statistics. Comments from R. Wanninkhof and two anonymous reviewers helped improve the manuscript. Financial support was provided by the LDEO Climate Center. LDEO contribution no. 6873.

References

Asher, W.E., Wanninkhof, R., 1998. The effect of bubble-mediated gas transfer on purposeful dual-gaseous tracer experiments. Journal of Geophysical Research 103 (C5), 10555–10560.

Brumley, B.H., Jirka, G.H., 1988. Air–water transfer of slightly soluble gases: turbulence, interfacial processes and conceptual models. Physicochem. Hydrodyn., vol. 10, pp. 295–319.

Caldwell, D.R., Elliott, W.P., 1971. Surface stresses produced by rainfall. Journal of Physical Oceanography 1 (2), 145–148.

Craeye, C., 1998. Radar signature of the sea surface perturbed by rain. PhD Thesis, Université Catholique de Louvain, Louvain-La-Neuve, Belgium, 311 pp.

Ho, D.T., Asher, W.E., Bliven, L.F., Schlosser, P., Gordan, E.L., 2000. On mechanisms of rain-induced air–water gas exchange. Journal of Geophysical Research 105 (C10), 24045–24057.

Ho, D.T., Bliven, L.F., Wanninkhof, R., Schlosser, P., 1997. The effect of rain on air–water gas exchange. Tellus 49 (2), 149–158.

Ho, D.T., et al., 2004. Influence of rain on air–sea gas exchange: lessons from a model ocean. Journal of Geophysical Research 109 (C08S18). doi:10.1029/2003JC001806.

Jähne, B., Huber, W., Dutzi, A., Wais, T., Ilmberger, J., 1984. Wind/wave-tunnel experiment on the Schmidt number—and wave field dependence of air/water gas exchange. In: Brutsaert, W., Jirka, G.H. (Eds.), Gas Transfer at Water Surfaces. D. Reidel, Norwell, MA, pp. 303–309.

Ledwell, J.R., 1984. The variation of the gas transfer coefficient with molecular diffusivity. In: Brutsaert, W., Jirka, G.H. (Eds.), Gas Transfer at Water Surfaces. Reidel, Hingham, Mass, pp. 293–302.

McGillis, W.R., et al., 2001. Carbon dioxide flux techniques performed during GasEx 98. Marine Chemistry 75, 267–280.

Meneghini, R., Kozu, T., 1990. Spaceborne Weather Radar. Artech House, Norwood, MA. 199 pp.

Poon, Y.-K., Tang, S., Wu, J., 1992. Interactions between rain and wind waves. Journal of Physical Oceanography 22 (9), 976–987.

Press, W.H., Flannery, B.P., Teukolsky, S.A., Vetterling, W.T., 1989. Numerical Recipes: The Art of Scientific Computing. Cambridge University Press, New York.

Tsimplis, M., Thorpe, S.A., 1989. Wave damping by rain. Nature 342 (6252), 893–895.

Tsimplis, M.N., 1992. The effect of rain in calming the sea. Journal of Physical Oceanography 22 (4), 404–412.

Wanninkhof, R., Ledwell, J.R., Broecker, W.S., Hamilton, M., 1987. Gas exchange on Mono Lake and Crowley Lake, California. Journal of Geophysical Research 92, 14567–14580.

Yang, Z.Z., Tang, S., Wu, J., 1997. An experimental study of rain effects on fine structures of wind waves. Journal of Physical Oceanography 27 (3), 419–430.